Remote Sensing of Environment 113 (2009) 213–223

Contents lists available at ScienceDirect

Remote Sensing of Environment

journal homepage: www.elsevier.com/locate/rse

Retrieving photometric properties of desert surfaces in China using the Hapke model and MISR data

Yunzhao Wu [a,b,*], Peng Gong [a,c], Qiang Liu [a], Adrian Chappell [d,1]

[a] State Key Laboratory of Remote Sensing Science, Jointly Sponsored by the Institute of Remote Sensing Applications of Chinese Academy of Sciences and Beijing Normal University, China
[b] School of Geophysical and Oceanographic Sciences, Nanjing University, Nanjing 210093, China
[c] Division of Ecosystem Science, University of California, Berkeley, CA 94720-3114, United States
[d] Centre for Environmental Systems Research, School of Environment & Life Sciences, University of Salford, Manchester, M5 4WT, UK

ARTICLE INFO

Article history:
Received 28 March 2008
Received in revised form 16 September 2008
Accepted 17 September 2008

Keywords:
Asymmetry factor
China
Desert
Hapke model
Inversion
MISR
Monte Carlo
Multi-angle remote sensing
Surface roughness
Sub-pixel

ABSTRACT

The retrieval of photometric properties of desert surfaces is an important first step in the parameterization of land surface components of regional dust emission and global radiation models and in Earth system modeling. In this study, the values of Hapke's photometric parameters (ω, h, b, c, $B0$, and $\bar{\theta}$) were retrieved from the Multi-angle Imaging SpectroRadiometer (MISR) instrument at locations in China's deserts. Four pixels represented the typical surface characteristics of the Taklimakan Desert, sand dunes of Kumtag Desert, relatively smooth areas of the Kumtag Desert and the aeolian sandy soil of Loulan. In contrast to earlier studies, we found that the retrieved parameter values were largely affected by the initial value. To combat this problem we used a Monte Carlo method with physical constraints and a conformity indicator to ensure physically meaningful inversion.

The results showed that the angular domain of MISR observations was sufficiently large to determine confidently the values of Hapke's photometric parameters with the exception of the opposition effect width (h). Retrieved values for the single scattering albedo (ω) and macroscopic roughness ($\bar{\theta}$) were consistent with qualitative observations about the structure and composition of the surface material and the nature of the dune forms, respectively. At Loulan, where the surface was smoother than other sites, retrieved values exhibited the strongest backward scattering. These results indicated that at the sensor scale, a rough surface (e.g., dunes) does not necessarily mean more backward scattering than a smooth surface. This finding has significant implications for empirical methods (e.g., using the normalized index of backward-scattered radiance minus forward-scattered radiance as an indicator to indicate surface roughness) which should be used carefully for analyzing surface roughness from remote sensing data. Future research is needed to 1) understand how surface roughness at the sub-pixel scale modifies the angular characteristics of reflectance and to 2) find practical methods for rapid whole image processing for mapping the photometric parameters.

1. Introduction

Formation and evolution of deserts can exert a significant influence on the climate system by altering surface albedo feedback and by supplying to the atmosphere and oceans mineral aerosols that affect the radiative balance of the atmosphere and the global carbon cycle (Ding et al., 2005; Li et al., 1995, 1996). Under an atmosphere largely transparent to solar radiation, desert areas provide a diversity of structure, composition, and spectral reflectance, and thereby affect the amount of solar radiation absorbed or reflected by the surface (Pinty et al., 1989). Removing the influence of illumination and viewing conditions on the reflectance provides photometric parameters such as the single scattering albedo (SSA), roughness and porosity of the surface etc., which provide consistent and repeatable photometric properties that may be diagnostic of the form and functions of deserts and other bare soil surfaces. Field measurements of these properties are sparse or infrequent because of the difficult and sometimes hazardous working conditions in many deserts. The synoptic view of satellite imagery enables researchers to quickly identify the spatial variation of photometric properties of deserts, especially for remote areas of sand seas (ergs). Moreover, repeated imaging of the same area permits the assessment of the dynamic nature of land surfaces with the potential for understanding the specific relationships between dune mobility, climatic variables, and human activity.

* Corresponding author. School of Geophysical and Oceanographic Sciences, Nanjing University, Nanjing 210093, China.
E-mail address: yzwu@yahoo.cn (Y. Wu).
[1] Current address: CSIRO Land and Water, GPO Box 1666, Canberra, ACT 2601, Australia.

0034-4257/$ – see front matter © 2008 Elsevier Inc. All rights reserved.
doi:10.1016/j.rse.2008.09.006

The directional scattering of light is a diagnostic characteristic of surface properties. Surface anisotropy can provide an additional source of information and a better understanding of the geophysical characterization of land surfaces. Anisotropic reflectance has been observed over various bare soil surfaces (Deering et al., 1990; Privette et al., 1995). The anisotropy may be rather complicated for desert areas due to the rising and falling sand ripples at the sub-pixel scales. Shoshany (1993) found with an empirical method that desert stone pavements produce anisotropic reflection with a clear backscattering regime. Karnieli and Cierniewski (2001) inferred the roughness of desert rocky surfaces from bidirectional reflectance data using a geometrical reflectance model. Cooper and Smith (1985) used a Monte Carlo soil reflectance model to study the effect of macroscopic surface irregularities. Although these studies described the Bidirectional Reflectance Factor (BRF) of soils well, the physical mechanisms responsible for the directional behavior of soils were not clear with these methods.

The bidirectional reflectance model derived by Hapke (1981, 1984, 1993, 2002) relates the radiance field emerging from a surface to physically meaningful parameters such as the SSA, the macroscopic roughness, and the porosity of the surface. Many studies have used the Hapke model for exploring planetary regolith, but relatively few attempts have been made to retrieve photometric properties of the Earth's surface (Chappell et al., 2006, 2007; Jacquemoud et al., 1992; Pinty et al., 1989; Privette et al., 1995). Bidirectional reflectance over arid surfaces is mainly influenced by the intrinsic spectral optical properties of the soil and by the presence of roughness elements (Escadafal, 1989). The generalized Hapke equation (1993, p. 346) with a roughness correction factor can be used to calculate the effects of macroscopic roughness on light scattered by a surface with an arbitrary diffuse reflectance function. Unfortunately, there have been no published studies of this type of Hapke model applied to Earth's surface despite numerous examples applied to the planetary regolith.

Owing to the advances in multi-angular imaging technology, space-borne multi-angle sensors such as Polarization and Directionality of the Earth Reflectances (POLDER) and Multi-angle Imaging SpectroRadiometer (MISR) provide the opportunities to acquire quickly off-nadir viewing data from space to assess the anisotropy of the surface components, and to improve the quantification of the structure of land surfaces. Most work with multi-angle sensors focus on vegetation rather than soils (e.g., Chen et al., 2003, 2005; Chopping et al., 2007; Pinty et al., 2002). Research on non-vegetated areas used the POLDER bidirectional reflectance product to develop an empirical relationship with aerodynamic roughness length which was mapped across desert surfaces (Laurent et al., 2005; Marticorena et al., 2004). Nolin and Payne (2007) extracted surface roughness of glacier ice from MISR data using an empirical relationship with the Normalized Difference Angular Index (NDAI). The advantages of the above empirical methods are that they provide quick and intuitively reasonable results but their physical meaning is unclear. For example, at the sensor scale, do rough surfaces produce more backward scattering of light than smooth surfaces?

There appear to be no published examples of retrieved photometric properties of the Earth's deserts from space-borne multi-angular data using Hapke's physical model. The MISR data and Hapke's macroscopic function (Hapke, 1993, p. 346) provide an opportunity to retrieve values of the photometric function and to derive physically meaningful parameters of the Earth deserts. Thus, the objective of this research is to investigate the utility of space-borne multi-angular MISR observations combined with the Hapke model to retrieve photometric properties of deserts in China.

Properties of sand dunes in the research area have been investigated by many workers (e.g., Liu et al., 2006; Wang et al., 2002; Wei et al., 2007). Additional information on soil types and properties was available in the 1:1,000,000 Soil Property Database of China. We also used the 1:2,000,000 Desert Distribution Map of China and 1:100,000 Desert Database of China to assist our research. Moreover, several Chinese scientists familiar with the research area provided additional valuable information. Although high-resolution aerial photography or field observations were not available, our results allow some preliminary conclusions to be drawn on the geophysical properties of the desert area, by means of a direct comparison with previous research results.

2. Methodology

2.1. Remotely sensed data

We used multi-angle remotely sensed data from MISR onboard NASA's Earth Observing System (EOS) Terra satellite launched in December 1999. The MISR instrument consists of nine cameras arranged with different view angles relative to the Earth's surface, and the along-track angles are 0° (nadir) for the An camera, and 26.1°, 45.6°, 60.0° and 70.5° forward and backward of nadir for the Af/Aa, Bf/Ba, Cf/Ca, and Df/Da cameras, respectively. Each of the nine cameras obtains images at four wavelengths in blue, green, red, and near-infrared that are centered at 446, 558, 672 and 866 nm, respectively. Over a 7-min interval, a particular location within the instrument swath is sequentially viewed by each of the nine MISR cameras. Thus, for an overpass each pixel is viewed at essentially the same solar geometry but nine different viewing angles. MISR Level 2 products (MIL2ASLS) obtained on 31 August 2007 were used in this study when the sky was clear of clouds. MISR Level 2 Surface products are 1100 m resolution and are screened for contamination from sources such as clouds, cloud shadows, sun glitter over water, topographically complex terrain, and topographically shadowed regions (Bothwell et al., 2002). A detailed description of the instrument can be found in Diner et al. (1998).

2.2. Study area

The study area coincides with MISR Path 140, Orbit number 40962, and Blocks 58–59 (Fig. 1). We chose this path because it contains two deserts: Taklimakan and Kumtag Desert which were historically separate but which now are almost contiguous to one another. The study of this area, therefore, is of great importance in understanding the wind activities and the dynamics of dune formation. The per pixel inversion of a physical model over an entire image is computationally expensive and often the model may not converge to a unique solution. To avoid this difficulty, representative locations were selected for careful analysis of the inversion procedure. The results were then compared with ancillary information about the surface characteristics. Three groups of pixels were chosen to represent three kinds of land surface in the research area (Fig. 1).

The first group (Group I: points A, D, and G) is in the Taklimakan Desert; the largest active desert in China and the second largest in the world (Wang et al., 2002). Group I represents the eastern portion of Taklimakan Desert. It is dominated by small 'simple' linear dunes with a N–S directional trend, an average height of <10 m and wide interdunes (ca. 300–1200 m wide) composed of aeolian sandy soils. Group II (points B, E, H, J, and K) is in the central-west area of Kumtag Desert. Dunes in this region are predominantly of the 'compound' linear type. The dunes are on average 10–50 m high, 50–100 m wide and 10–20 km long. Points B, H, and J represent the sand dune area of the Kumtag Desert, and points E and K represent the relatively smooth and level area of the Kumtag Desert, which is regarded as peripheral to the Gobi Desert (pseudo-Gobi) by some scientists. Group III (points C, F, and I) is about 42 km to the east of the ancient city of Loulan (now not evident) and which we named Loulan in the analysis. Group III is not regarded as desert now but it has an aeolian sandy soil type.

The black and white images from China–Brazil Earth Resources Satellite (CBERS, spatial resolution is 19.5 m) for points A, B, E, and C are shown in Fig. 2a, b, c, and d, respectively. The images show that the land surface is the smoothest for Loulan (Fig. 2d) while the roughest for the sand dunes (Fig. 2a and b). The angular information of the 9 cameras

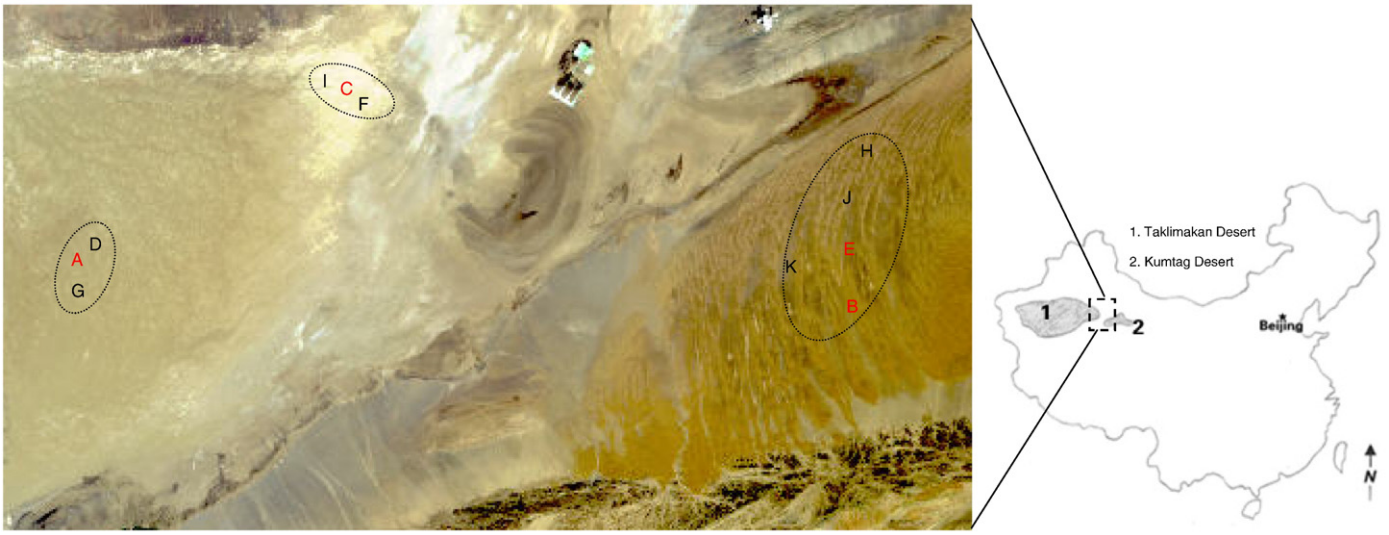

Fig. 1. MISR (Level 1 product) nadir true color map (275 m spatial resolution) showing the three groups used in this study. The points in red are the pixels used for inversion. (For interpretation of the references to color in this figure legend, the reader is referred to the web version of this article.)

and BRF in the red bands for these four points are shown in Table 1. The solar zenith angle (SZA) is given by *i*, the view zenith angle (VZA) is given by *e*. The relative azimuth angle between the sun and the viewer is given by RAA and *g* is the phase angle between the incoming and outgoing light directions. Values of RAA in Table 1 show that the flight of the MISR instrument is an oblique orbit.

2.3. Hapke model description

We combined the model of Hapke (1993, p. 346) that includes a macroscopic roughness parameter with that of Hapke (2002) that uses a numerical approximation of multiple light scattering to allow for anisotropic phase functions. Hapke's model calculates the bidirectional

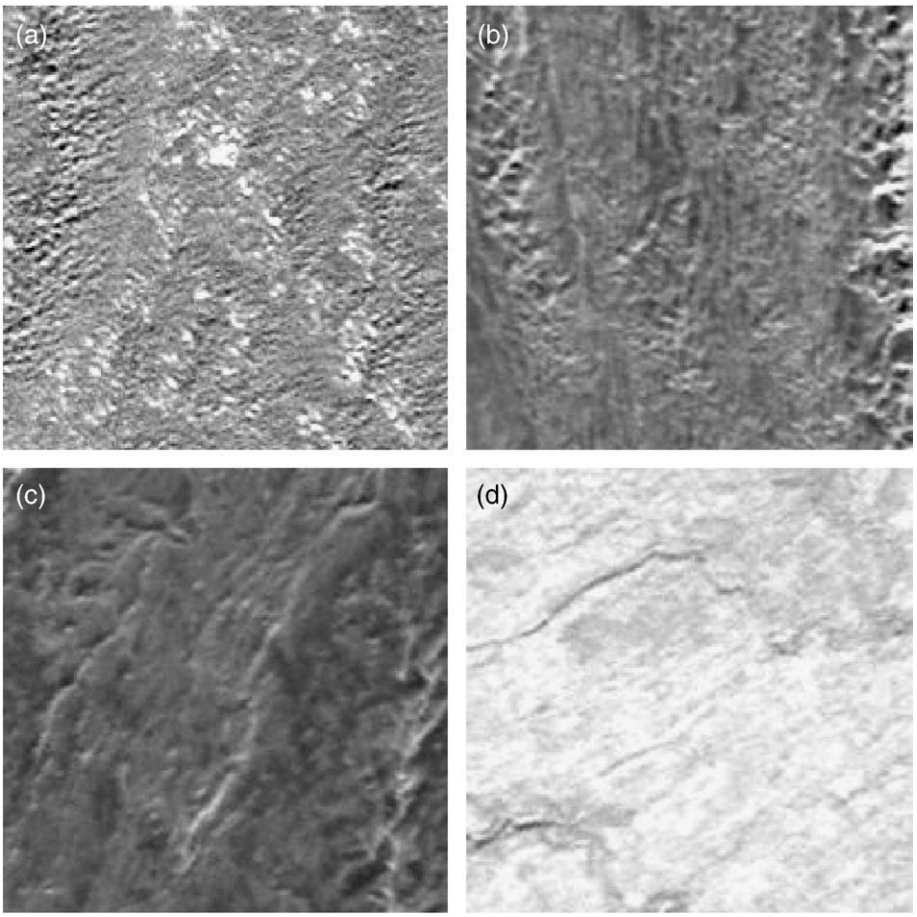

Fig. 2. The 19.5 m CBERS images covering an area of 3.6 km×3.6 km (200×200 pixels) for point A (a), point B (b), point E (c) and point C (d). The center of each image (56×56 pixels) corresponds to the MISR pixel of the four points. The flat areas (a) are the low areas between dunes (interdunes). The white points (a) are the bare aeolian sandy soils, similar to those at Loulan (d).

Table 1
Location and angular information for the four points used for the inversion

	e	*i*	RAA	*g*	BRF	*e*	*i*	RAA	*g*	BRF
	A (40°4′47.65″, 88°47′8.49″)					B (39°40′21.7″, 91°43′27.81″)				
Df	70.581	34.870	129.950	94.212	0.275	70.134	33.340	143.432	97.542	0.263
Cf	60.525	34.870	127.545	84.238	0.281	60.111	33.340	145.466	88.638	0.259
Bf	46.541	34.870	123.229	70.310	0.290	46.029	33.340	149.876	76.237	0.251
Af	28.217	34.870	112.616	51.756	0.286	27.789	33.340	161.873	60.294	0.243
An	10.995	34.870	46.053	28.229	0.275	12.521	33.340	129.984	42.355	0.237
Aa	27.591	34.870	24.335	14.439	0.304	29.005	33.340	67.576	33.664	0.254
Ba	46.075	34.870	35.337	25.167	0.313	46.996	33.340	56.437	37.626	0.264
Ca	60.306	34.870	39.708	37.955	0.311	60.897	33.340	52.153	45.494	0.270
Da	70.557	34.870	42.059	47.672	0.316	71.059	33.340	50.041	52.768	0.274
	E (39°53′11.83″, 91°46′47.08″)					C (40°30′17.68″, 89°52′18.97″)				
Df	70.131	33.610	143.559	97.801	0.210	70.264	34.788	134.598	95.724	0.362
Cf	60.099	33.610	145.531	88.879	0.206	60.095	34.788	133.551	86.062	0.389
Bf	45.997	33.610	149.823	76.446	0.206	45.732	34.788	131.857	72.504	0.409
Af	27.689	33.610	161.559	60.433	0.205	26.335	34.788	127.778	54.480	0.421
An	12.206	33.610	129.710	42.335	0.204	3.718	34.788	46.007	32.303	0.429
Aa	28.883	33.610	66.774	33.419	0.218	26.287	34.788	37.419	20.444	0.454
Ba	46.943	33.610	55.863	37.291	0.226	45.714	34.788	41.480	28.425	0.482
Ca	60.870	33.610	51.687	45.156	0.232	60.192	34.788	43.122	39.683	0.502
Da	71.041	33.610	49.636	52.438	0.235	70.539	34.788	44.079	48.695	0.527

RAA: Relative azimuth angle between the incidence and emergence angles.
BRF: The BRF of the red band extracted from MISR data.

reflectance (r) while the usual outcome of measurements in the laboratory or from satellite is BRF. The BRF = $\pi r/\cos(i)$ and the combined Hapke model is:

$$R(i,e,g) = \frac{\omega}{4}\frac{1}{\mu_{0e}+\mu_e}\{[1+B(g)]P(g)+M(\mu_{0e},\mu_e)\}S(i,e,g,\bar{\theta}) \quad (1)$$

where

$$B(g) = \frac{B0}{1+(1/h)\tan(g/2)}$$

$$M(\mu_{0e},\mu_e) = P(\mu_{0e})[H(\mu_e)-1]+P(\mu_e)[H(\mu_{0e})-1]+P[H(\mu_e)-1][H(\mu_{0e})-1]$$

$$P(x) = 1+\sum_{n=1}^{\infty} A_n b_n P_n(x)$$

$$P = 1+\sum_{n=1}^{\infty} A_n^2 b_n$$

$A_n = 0$ n even,

$$A_n = \frac{(-1)^{\frac{n+1}{2}}}{n}\frac{1\cdot 3\cdot 5\cdot n}{2\cdot 4\cdot 6\cdot (n+1)}\ n \text{ odd},$$

and the terms b_n are the Legendre expansion coefficients of the phase function:

$$p(g) = 1+\sum_{b=1}^{\infty} b_n p_n \cos(g)$$

$$H(x) = \left\{1-[1-\sqrt{1-\omega}]x\left[r_0+\left(1-\frac{1}{2}r_0-r_0x\right)\ln\left(\frac{1+x}{x}\right)\right]\right\}^{-1}$$

$$r_0 = \frac{2}{1+\sqrt{1-\omega}}-1$$

In Eq. (1), ω is the single scattering albedo, B is the opposition effect function, P is the phase function, and M is an approximation of multiple scattering for anisotropic phase functions which differs by less than 1% from more sophisticated calculations (Hapke, 2002). The macroscopic roughness function S is given in Hapke (1993, p. 344–345) and contains the macroscopic roughness parameter angle ($\bar{\theta}$). The cosine of effective angle of incidence and angle of emergence μ_{0e} and μ_e, respectively, are calculated using the equations by Hapke (1993, p. 344–345).

Legendre polynomials and the Henyey–Greenstein function are usually used in radiative transfer models. Although the accuracy increases as the order of $P(g)$ increases, the problem of uniquely determining values of the parameters also increases. After many trials our preliminary results revealed that a second-order Legendre polynomial series,

$$P_L(g) = 1+b\cos g+c(3\cos^2 g-1)/2 \quad (2)$$

and a double Henyey–Greenstein (HG) function,

$$P_{HG}(g) = \frac{1+b}{2}\frac{1-c^2}{[1+2c\cos g+c^2]^{3/2}}+\frac{1-b}{2}\frac{1-c^2}{[1-2c\cos g+c^2]^{3/2}} \quad (3)$$

were most appropriate for this study. The final formulation of the Hapke model we used contains the following six parameters: ω, h, b, c, $B0$, and $\bar{\theta}$, which have been summarized in Table 2. The optimum values of the six model parameters will be established by inverting the model against the angular measurements of reflectance from the MISR Level 2 BRF product.

Table 2
Description of the parameters of Hapke model used in this study

Symbol	Description
ω	Single scattering albedo which is defined as the ratio of the amount of light at a given wavelength scattered from a representative incremental volume of a medium to the combined amount of light scattered from and absorbed by it
h	Angular-width parameter of opposition effect
b	Coefficients in phase function (see formula (2) and (3))
c	
$B0$	Amplitude of opposition effect. Both $B0$ and h characterize is the non-linear increase in brightness with decreasing phase angle observed near $g=0$.
$\bar{\theta}$	Macroscopic roughness correction factor which is the mean topographic slope angle of surface roughness at subresolution scale

Table 3
Parameter constraints used in this study

	$P_L(g)$	$P_{HG}(g)$
ω	0.01–1	0.01–1
h	0.01–2	0.01–2
b	−1.5–1.5	$P_{HG}(g)>0$
c	$P_L(g)>0$	0–1
$B0$	0.01–1	0.01–1
$\bar{\theta}$	0–60°	0–60°

2.4. Inversion of Hapke model

This Hapke model is highly non-linear and contains six model parameters that combined making it difficult for the inversion procedure to find unique meaningful solutions. Without *a priori* information on the parameter values the inverse problem typically consists of determining the optimal set of variables that minimizes the distance between observations and modeled values with the iterative numerical calculation. A non-linear least squares fitting procedure was used to solve the inverse problem. The performance of the optimization was judged using the square root of mean squared error (RMSE), defined as:

$$\mathrm{RMSE} = \sqrt{\sum_{k=1}^{n} [r_k - r(i_k, e_k, g_k)]^2 / N_f} \quad (4)$$

where r_k is the measured BRF for the relative geometry of illumination and observation defined by i_k, e_k, g_k. The total number of observations is n and r is the calculated BRF. The number of degrees of freedom N_f is the number of independent data points minus the number of parameters estimated by the procedure.

The iterative numerical approaches to determine best-fit parameters require initial parameter values. Helfenstein and Veverka (1987) used a plausible first-guess of model parameters to compute the initial value. Pinty et al. (1989) and Chappell et al. (2006) found that the values of the retrieved model parameters and of RMSE did not depend on the initial estimate. However, their inversion experiments used only a few initial simulated values. We used many parameters with many different initial values and found that the inversion results were significantly influenced by the initial values. For example, some initial values gave solutions with large RMSEs whilst some did not converge to a solution. Our results (unpublished data) showed that interpretation of the photometric parameter values is highly dependent on the careful determination of the initial value. This is also one of the reasons why we focused on only a few detailed locations before attempting to invert an entire image of reflectance data against the model.

We used a Monte Carlo method to determine the initial values. For each inversion, the starting position was prescribed randomly. Since some starting positions did not converge to a solution, more than 300 trials were used to ensure that 300 results were acquired in each case. The criterion of an acceptable optimal solution was determined with the lowest RMSE and with physically reasonable meaning. In addition, some parameter constraints were applied to prevent physically implausible solutions. The parameter limits in Table 3 were established based on the outcome of the experiments and after a review of previous results (Jacquemoud et al., 1992; McGuire & Hapke, 1995; Privette et al., 1995). Parameter b in $P_L(g)$ was constrained between −1.5 and 1.5 because we believed that the asymmetry factor $\xi = <\cos(\pi - g)> = -b/3$ should be between −0.5 and 0.5 for densely packed particles. The partition coefficient parameter b in $P_{HG}(g)$ has been constrained elsewhere often between −1 and 1 (e.g., Cord et al., 2003; Shepard & Helfenstein, 2007). We tested this condition in this study. We also tested $P_{HG}(g)$ with an additional constraint on b, i.e., we kept $P_{HG}(g)>0$, to find an improved constraint on b for future studies by comparing the accuracy of the inversion. Regardless of whether $P_{HG}(g)$ or $P_L(g)$ is used, workers should note that the phase function must be constrained to ensure $P(g)>0$ because even though the inversion procedure can lead to smaller RMSE with $P(g)<0$, such results are physically meaningless.

The parameter constraints, definition of a physically meaningful value and use of the smallest RMSE ensured that we acquired parameter values that were meaningful. However, different combinations of physically meaningful parameters produced similar RMSE. To tackle this additional problem we developed a method, here named a conformity indicator, which we adopted to choose the optimal solution in the presence of similarly small RMSE values. For example, all 300 solutions of the inversion for the Taklimakan Desert using the green band and $P_L(g)$, showed that there were 43 occurrences of $0<\xi$, and 257 occurrences of $\xi<0$. We chose the latter because it had the largest frequency of occurrences which we believed indicated the highest probability of being correct.

Earlier studies reported that when the phase angle (g) is greater than 20°, the effect of the opposition surge can be negligible (Cord et al., 2003; Mustard and Pieters, 1989; Piatek et al., 2004). As shown in Table 1 the phase angles of our data are mostly greater than 20° except for point A which has the smallest value ($g=14.44°$). To demonstrate the reliability of the previously retrieved parameter values we repeated the inversion procedure without the opposition surge effect by using only four parameters (ω, b, c, and $\bar{\theta}$). The fewer number of parameters would be more convincingly retrieved than six parameters. Hence the parameter values (including the asymmetry factor and RMSE) of the full parameter set were compared with those of the reduced parameter set.

We performed the inversion using each of the bands and found that the BRFs in the blue band were different from those in the remaining 3 bands. This was believed to be due to the stronger atmospheric effects in the blue band in comparison with the other bands. Consequently, we inverted the model initially against only the green, red, and NIR bands separately. Theoretically, phase function and roughness parameters vary with wavelength. However, many researchers regarded all the parameters in the Hapke model except ω to be independent of the wavelength (Chappell et al., 2006, 2007; Jacquemoud et al., 1992). We considered the parameters to be constant and fit them globally at the same time as the three ω corresponding to the three wavebands.

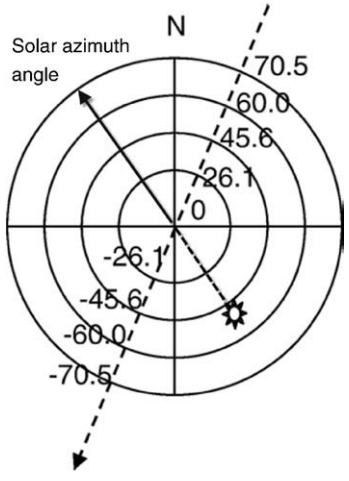

Fig. 3. Explanation of view angles and solar azimuth angle defined by MISR. Please note that the definition of solar azimuth angle is pointing away from the Sun, which is contrary to the convention used in the Hapke formulation. So when calculated for the Hapke model the RAA should have 180° subtracted.

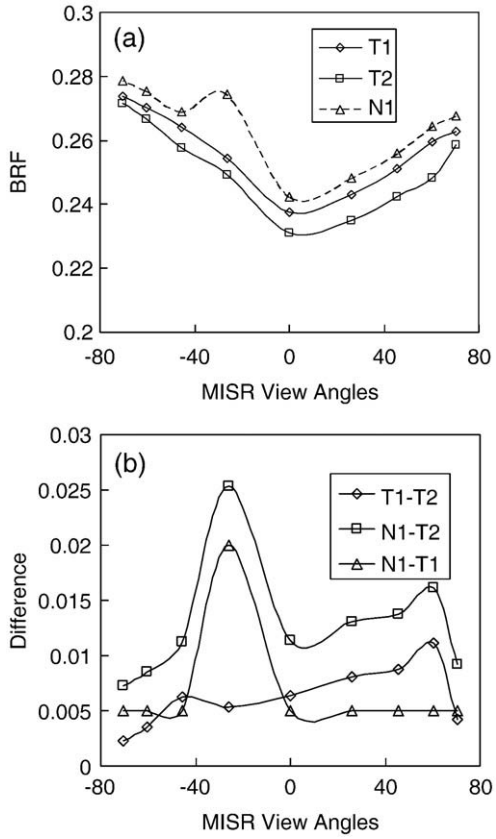

Fig. 4. Bidirectional reflectance factor of true pixels (T1 and T2) extracted from two adjacent pixels of MISR data and the simulated data (N1) with large noise at the −26.1° observing angle (a), and the difference of BRF between the three points (b). The Grubbs' test results for the difference between the three points were shown in Table 4.

Prior to inversion of the model against the reflectance data we ascertained that the SZA, VZA and RAA were required. The values of these parameters are available per pixel from the MISR L2 products. Users of MISR data should note that RAA is provided following a different convention to that of some radiative transfer models. Solar azimuth angles of MISR data are defined pointing away from the Sun, not toward it. The solar azimuth angle for our data is given in the MISR product as 331° (Fig. 3). According to the convention used in the Hapke formulation, the RAA should have 180°subtracted. Otherwise, the hot spot will be in the opposite direction.

2.5. Testing the significance of noise in MISR data

Pinty et al. (1989) and Chappell et al. (2006) found the RMSE of inversion for synthetic data (clean data) to be very small. Our experiments (unpublished data) also found very small RMSE values (typically 1×10^{-5}) with the 9-angular simulated data closely resembling the illumination and viewing geometry of MISR data. The RMSE became large for noisy data (Pinty et al., 1989; Chappell et al., 2006). The amount of noise in our MISR data was tested with the Grubbs' test (Grubbs 1969; Stefansky, 1972). The intention was to ensure that the intended points for the inversion had sufficiently small noise to retrieve meaningful results.

Table 4
Grubbs' test results for the difference between the three points

Observing angle(°)	T1–T2	N1–T2	N1–T1	critical value
70.5	0.726	0.679	0.333	
60.5	1.776	0.601	0.333	
45.6	0.896	0.151	0.333	
26.1	0.676	0.038	0.333	
0	0.070	0.271	0.333	2.21 (confidence interval: 0.95) 2.39 (confidence interval: 0.99)
−26.1	0.315	**2.297**	**2.667**	
−45.6	0.015	0.300	0.333	
−60.5	0.976	0.806	0.333	
−70.5	1.415	1.031	0.333	

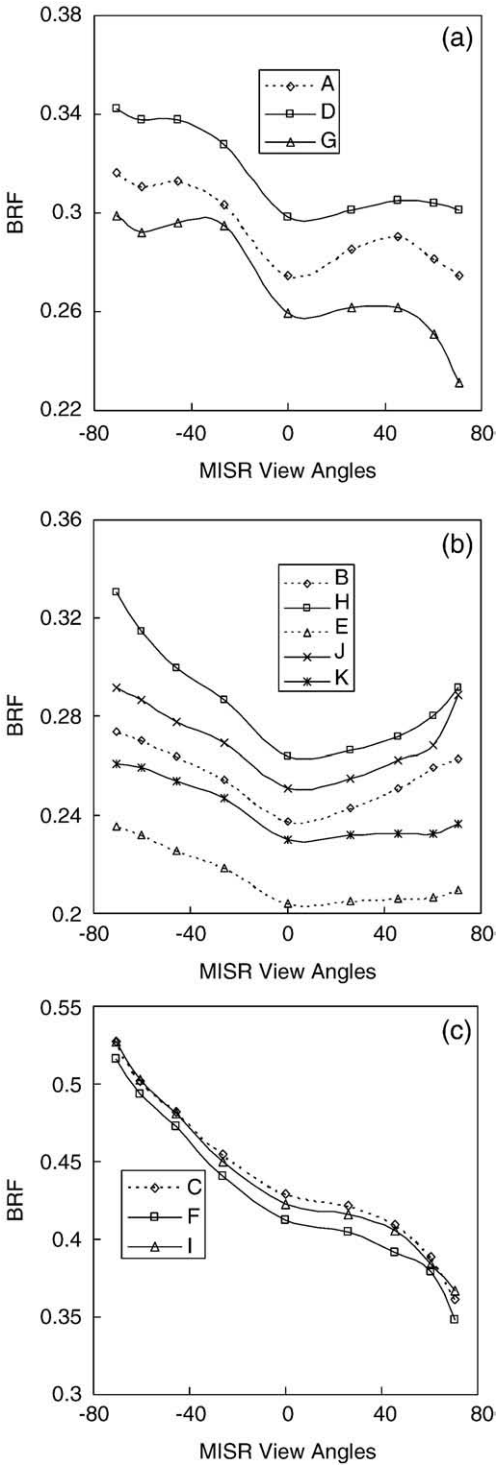

Fig. 5. Angular signatures of MISR bidirectional reflectance factor for Group I (a), Group II (b), and Group III (c) in red band. The dotted line is the data used for the inversion.

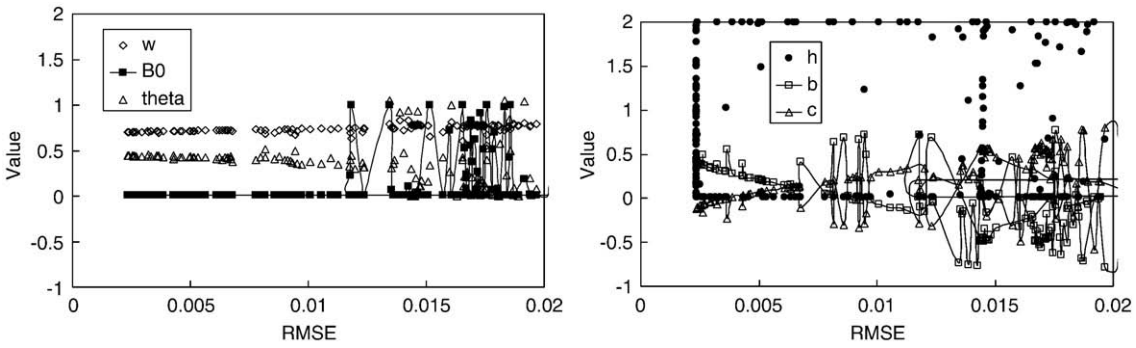

Fig. 6. The retrieved values of the six parameters of Hapke model against the RMSE for point B for red band with $P_L(g)$ phase function. It indicates that in case of the smallest RMSE (e.g. <0.005), ω and $B0$ has the lowest uncertainty, next is $\bar{\theta}$, while h has the largest uncertainty of inversion.

Grubbs' test is defined for the null hypothesis H_0: There are no outliers in the data set and the alternative hypothesis H_a: There is at least one outlier in the data set. The Grubbs' test statistic is defined as:

$$\frac{G = \max|Y_i - \bar{Y}|}{s} \tag{5}$$

with Y denoting the i values and $\bar{Y}$ and s are the sample mean and standard deviation, respectively. For the two-sided test, the hypothesis of no outliers is rejected if

$$G > \frac{N-1}{\sqrt{N}} \sqrt{\frac{t^2_{(\alpha/(2N),N-2)}}{N-2+t^2_{(\alpha/(2N),N-2)}}} \tag{6}$$

with $t^2_{(\alpha/(2N),N-2)}$ denoting the critical value of the t-distribution with $(N-2)$ degrees of freedom and a significance level of $\alpha/(2N)$. For the one-sided tests, a significance level of α/N was used.

Fig. 4 is an example of the noise test applied to the MISR data. T1 is the true pixel extracted from MISR data (point B). The type of land cover of the desert areas is relatively simple with a dominance of sand. Around T1, there are points with a similar land surface. T2 is one of the true values extracted from MISR data adjacent to T1. N1 is the simulated data with large noise at the −26.1° observing angle. Because the land surface is similar, the shapes of the BRFs of the points should be similar. Fig. 4b is the difference of BRF between the three points. It can be seen that the difference between the two true values is small. They have a large difference when compared to the synthetic noisy data (N1) at the −26.1° observing angle. Table 4 showed that both Grubbs test values exceed the 0.95 confidence interval, while T1 and T2 are tolerable. With this method the noise tests were performed for all the pixels used in the following inversion.

3. Results

3.1. Bidirectional reflectance of the three sites

Fig. 5a–c shows the BRFs of the three groups of pixels in the red band. Negative view angles indicate backward scattering of light. In general, the shape of the BRFs for the two deserts exhibits the common 'bowl' shape (i.e., the BRF is lower at nadir than at larger viewing angles). The backward scattering is slightly more prominent for the Taklimakan Desert. The most obvious difference in the BRF between the two deserts is that the two most forward cameras (Cf and Df) decrease for the Taklimakan Desert while they increase for the Kumtag Desert (Fig. 5a and b). At Loulan the BRF is very different from those of the deserts. The BRFs for each pixel show considerably larger reflectance and exhibit larger backward scattering than in the deserts (Fig. 5c). The BRF decreases gradually at the more forward observing angles.

In the inversion we used the following pixel(s) to represent each group: point A for Group I, points B and E for Group II, and point C for Group III. The four points (Fig. 2) were chosen to represent the widely contrasting land surface conditions including the bright aeolian sandy soil (point C), small dunes with wide interdune areas primarily composed of aeolian sandy soils (point A) and flat and dark interdune areas (point E), and sand dunes (point B). The Grubbs' test showed that the four points all had values which did not exceed the 0.95 confidence interval and are here considered to have undetectable levels of noise (unpublished data).

3.2. Inversion results from the full parameter set

While the forward problem has a unique solution, the inverse problem does not. For example, given a set of value of Hapke's parameters, we can uniquely predict the BRF, but there are different combinations of values for Hapke's parameters that give the same BRF. Therefore, the inverse problem has multiple solutions. To assess the

Table 5
Values of Hapke parameters retrieved from the full parameter set

	ω	h	b	c	$B0$	$\bar{\theta}$(°)	ξ	RMSE
$P_L(g)$								
Green band								
A	0.616	0.121	0.802	−0.198	0.010	25.854	−0.267	0.004
B	0.539	0.010	0.539	−0.201	0.010	25.968	−0.179	0.003
E	0.490	0.448	0.717	−0.213	0.010	24.248	−0.239	0.005
C	0.798	1.982	1.017	0.016	0.010	16.854	−0.339	0.018
Red band								
A	0.685	1.956	0.809	−0.191	0.010	26.083	−0.269	0.006
B	0.657	0.140	0.554	−0.184	0.010	25.510	−0.185	0.002
E	0.576	1.704	0.717	−0.196	0.010	25.280	−0.239	0.004
C	0.858	0.010	1.042	0.042	0.010	15.936	−0.347	0.021
NIR band								
A	0.722	0.128	0.728	−0.190	0.010	25.395	−0.243	0.007
B	0.702	0.011	0.434	−0.116	0.010	25.395	−0.145	0.002
E	0.614	1.887	0.619	−0.171	0.010	24.019	−0.208	0.006
C	0.870	0.018	1.035	0.035	0.010	15.592	−0.345	0.020
$P_{HG}(g)$								
Green band								
A	0.610	0.052	−5.009	0.034	0.010	23.446	−0.169	0.008
B	0.545	0.011	−5.825	0.016	0.010	24.592	−0.098	0.005
E	0.495	0.091	−4.938	0.031	0.010	22.127	−0.151	0.006
C	0.754	0.536	−5.581	0.060	0.010	6.592	−0.337	0.012
Red band								
A	0.673	0.052	−5.676	0.031	0.010	23.446	−0.177	0.011
B	0.655	0.347	−6.533	0.016	0.010	23.675	−0.107	0.005
E	0.573	1.692	−4.617	0.034	0.010	23.217	−0.156	0.006
C	0.805	0.557	−5.108	0.069	0.010	7.121	−0.350	0.011
NIR band								
A	0.713	0.123	−5.738	0.025	0.010	22.758	−0.145	0.009
B	0.695	0.074	−6.732	0.014	0.010	23.904	−0.093	0.004
E	0.611	1.430	−3.913	0.034	0.010	21.726	−0.132	0.006
C	0.818	1.374	−5.666	0.059	0.010	6.433	−0.336	0.012

Table 6
Values of Hapke parameters retrieved using multi-bands from the full parameter set

	h	b	c	$B0$	$\bar{\theta}$	ξ	RMSE
$P_L(g)$							
A	0.121	0.795	−0.204	0.010	25.854	−0.265	0.005
B	0.131	0.503	−0.162	0.010	25.553	−0.168	0.002
E	0.448	0.718	−0.204	0.010	24.879	−0.239	0.003
C	0.013	1.039	0.039	0.010	15.707	−0.346	0.013
$P_{HG}(g)$							
A	0.700	−5.799	0.029	0.010	23.434	−0.168	0.005
B	0.010	−7.191	0.014	0.010	23.950	−0.101	0.003
E	0.361	−4.937	0.032	0.010	22.802	−0.157	0.003
C	0.010	−18.873	0.019	0.010	6.482	−0.359	0.004

stability expected for each parameter, we have presented the retrieved values against the RMSE for point B using $P_L(g)$ as an example (Fig. 6). The uncertainties for the parameters were estimated from the standard deviations of the smallest RMSE (e.g. <0.005). The uncertainties are ±0.003 for ω, 0.65 for h, 0.055 for b, 0.046 for c, 0.0001 for $B0$, and 0.005 for $\bar{\theta}$. In the case of the smallest RMSE, the most stable parameters (i.e., those with the smallest uncertainty) are ω and $B0$ (Fig. 6). We found that $\bar{\theta}$ is also quite robust with most of the values near 25.21° (0.44 in radian). The angular-width parameter of the opposition effect, h, has the largest uncertainty among the six parameters with values from the lower to upper limits. Fig. 6 shows the stability of Hapke's parameters and also suggests that our conformity indicator is a reasonable method to determine the best solution.

The optimized values of each model parameter for each pixel location (land surface type) and for each band are listed in Table 5 for the two phase functions. The asymmetry factor ξ, which is often used to characterize the angular-scattering regime, is also presented in Table 5. Negative values of ξ indicate preferential backscattering, while positive ones represent forward scattering. Regardless of the phase functions used in the model inversion and the locations, all parameters except ω and h are similar for all three bands used. Furthermore, the results show that amongst the four pixels the values of the parameters are different. The results from the multi-band inversion are listed in Table 6. Initial values came from approximations based on previous single band inversion (Table 5). The accuracy of the inversion using all bands was slightly increased and the values of the parameters for the three land surfaces were similar for single band and multi-bands. Fig. 7 shows the measured and modeled BRF with the optimal model for the four points. The model reproduces well the angular configurations.

Despite the fact that the orbit of MISR is not in the principal plane and that its viewing angles are limited in number, the single scattering albedo, phase function, topographic shadowing function as well as opposition surge parameters (except h) can be retrieved well. Fig. 6 and Tables 5 and 6 showed that the retrieved $B0$s for all the points are all very small and close to the smallest parameter constraint, which is consistent with the fact that the phase angle was too large to detect the opposition effect (Table 1). The opposition surge width h does not influence the BRF. We believe that this is largely due to the low amplitude of the small $B0$. This explains why the h parameter has such large uncertainty. Since $B0$ is very small in MISR phase angles, it is not feasible to estimate h without *a priori* knowledge.

3.3. Inversion results from the reduced parameter set

The results of the inversion for the reduced parameter set (four parameters) are shown in Table 7 for a single band and in Table 8 for multiple bands. We compared the values of the coincident parameters (including the asymmetry factor and RMSE) in the full parameter set (Table 5) with those of the reduced parameter set (Table 7). The retrieved values for all of the coincident parameters were very similar. This gave considerable confidence that our retrieved values of the full parameter set were correct. It supported our conclusion above that even with the limited set of angular samples, the full set of Hapke parameters can be retrieved from the MISR data. Consequently, we will focus the discussion of the results primarily on the 4 parameters (Tables 7 and 8).

Both phase functions gave similar accuracy for all the points except for point C. For point C, $P_{HG}(g)$ was more accurate than $P_L(g)$, but the former phase function requires much longer computational time than $P_L(g)$. It should be noted that for $P_{HG}(g)$ the partition coefficient b was

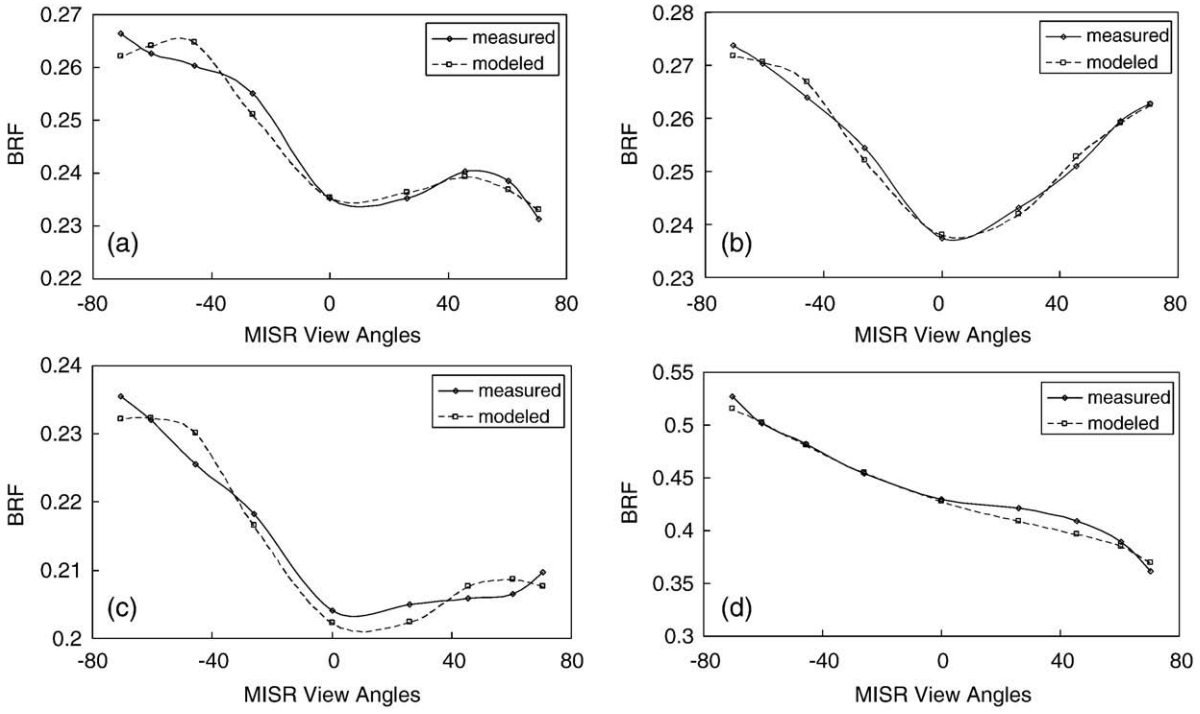

Fig. 7. Modeled and measured MISR data with the optimal model for (a) point A (b) point B (c) point E and (d) point C.

Table 7
Values of Hapke parameters retrieved from the reduced parameter set

	ω	b	c	$\bar{\theta}$	ξ	RMSE
$P_L(g)$						
Green band						
A	0.617	0.804	−0.196	25.898	−0.268	0.004
B	0.539	0.540	−0.201	26.012	−0.180	0.003
E	0.491	0.720	−0.211	24.293	−0.240	0.004
C	0.800	1.020	0.020	16.845	−0.340	0.017
Red band						
A	0.687	0.811	−0.189	26.070	−0.270	0.005
B	0.658	0.555	−0.182	25.497	−0.185	0.002
E	0.578	0.720	−0.195	25.267	−0.240	0.003
C	0.859	1.043	0.043	15.986	−0.348	0.019
NIR band						
A	0.723	0.725	−0.185	25.439	−0.242	0.006
B	0.702	0.434	−0.116	25.382	−0.145	0.002
E	0.616	0.623	−0.170	24.007	−0.208	0.005
C	0.870	1.035	0.035	15.584	−0.345	0.018
$P_{HG}(g)$						
Green band						
A	0.609	−6.812	0.025	23.549	−0.172	0.006
B	0.545	−3.628	0.027	24.580	−0.099	0.004
E	0.498	−1.993	0.072	22.116	−0.143	0.005
C	0.747	−13.216	0.027	4.305	−0.361	0.009
Red band						
A	0.672	−5.736	0.031	23.434	−0.180	0.009
B	0.655	−2.681	0.039	23.663	−0.109	0.004
E	0.574	−6.760	0.023	23.262	−0.159	0.004
C	0.801	−13.734	0.027	4.027	−0.370	0.009
NIR band						
A	0.712	−4.841	0.030	22.861	−0.148	0.008
B	0.695	−3.359	0.028	23.892	−0.094	0.003
E	0.613	−2.672	0.049	21.658	−0.131	0.005
C	0.815	−19.163	0.019	4.381	−0.363	0.008

not between −1 and 1, i.e., the best solution was given without constraints on b. To show the effects of the constraints on the inversion, we made one additional experiment using point C. This experiment involved b with constraints between −1 and 1. The optimum result was $b=-1$ with the lowest RMSE=0.02, which is 2.4 times larger than for the RMSE with no limitation. This result indicates that the inversion is best performed without constraining the partition coefficients except keeping $P_{HG}(g)>0$.

All the values of single scattering albedo, macroscopic roughness, and asymmetry parameters retrieved using $P_{HG}(g)$ were a little lower than those of $P_L(g)$. Regardless of which phase function was used in the inversion, all the parameters showed approximately the same trends for the four points. For example, the order of the four points for the single scattering albedo is C>A>B>E, and for the asymmetry factor (absolute value) is C>A>E>B. The order for the average macroscopic roughness parameter $\bar{\theta}$ is A or B>E>C. The macroscopic roughness parameter of point A is larger than B for $P_{HG}(g)$, however, there is some difference for its order for $P_L(g)$. The values at Loulan of $\bar{\theta}$ acquired using the two phase functions are very different: 4.58° for $P_{HG}(g)$ and 16.04° for $P_L(g)$. The value of $\bar{\theta}$ from $P_{HG}(g)$ appears to be more acceptable because its RMSE is much smaller than that of $P_L(g)$. Regardless of which phase function was used, Loulan consistently has the smallest $\bar{\theta}$ and the two deserts (points A and B) have larger and similar values.

The asymmetry factor of the phase function showed the angular-scattering characteristics expected from Fig. 5a–c. The largest negative values of ξ were evident for Loulan. The Taklimakan Desert and the relatively flat area of Kumtag Desert (point E) have moderately negative ξ. The sand dune area of the Kumtag Desert (point B) has marginally negative ξ. Thus, Loulan has the strongest backscattering, Taklimakan Deserts and the flat area of Kumtag Desert have moderate backscattering, the sand dune area of the Kumtag Desert has the weakest backscattering of all the land surface types.

Table 8
Values of Hapke parameters retrieved using multi-bands from the reduced parameter set

	b	c	$\bar{\theta}$	ξ	RMSE
$P_L(g)$					
A	0.807	−0.193	26.070	−0.269	0.003
B	0.549	−0.190	25.669	−0.183	0.002
E	0.720	−0.202	24.866	−0.240	0.003
C	1.032	0.032	16.043	−0.344	0.015
$P_{HG}(g)$					
A	−18.834	0.009	23.434	−0.170	0.005
B	−13.414	0.008	24.064	−0.103	0.007
E	−13.033	0.012	21.772	−0.156	0.003
C	−27.101	0.014	4.584	−0.366	0.007

4. Discussion

Although the estimate of the opposition surge width h has a large uncertainty, the results indicate that variation in other Hapke photometric parameter values is diagnostic of differences in the physical structure of the land surface. They support previous studies in their assertion that these diagnostic characteristics can be associated with meaningful geophysical properties (Chappell et al., 2006, 2007; Jacquemoud et al., 1992; Pinty et al., 1989; Privette et al., 1995).

Compared to the desert sites, the Loulan surface shows a very reflective surface comprising aeolian sandy soil (1:1000,000 Soil Property Database of China). This finding is consistent with the largest ω values at Loulan amongst the three land surfaces. Point E, which is regarded as the periphery of the Gobi Desert (pseudo-Gobi) by some scientists, is composed of dark sand gravel (Fig. 8a). This is consistent with the smallest ω values. Besides quartz and feldspar, the sand

Fig. 8. Digital photo of the periphery of the Gobi Desert (pseudo-Gobi) landscape (a) and a laboratory photo of the Kumtag Desert sands (b).

dunes of the Kumtag Desert (point B) contain hornblende, magnetite and other dark minerals (Fig. 8b). The Taklimakan surface (point A) shows small and low linear dunes with wide and flat interdune areas which comprise mainly aeolian sandy soils (Fig. 2a) and fine grain size (Wei et al., 2007) which explain the finding of a larger ω value for the Taklimakan than for the Kumtag Desert surfaces.

Our results had $\bar{\theta}$ between 4° and 26°, similar to values extracted from solar system objects (Clark et al., 2002; Helfenstein and Veverka 1987) and smooth surfaces in the laboratory (Cord et al., 2003; Shepard & Helfenstein, 2007). However, in the derivation of $\bar{\theta}$, the albedo is assumed to be sufficiently small that multiple scattering between surface facets can be neglected, whereas deserts have large albedo values. Therefore, $\bar{\theta}$ may be an underestimate of the actual value. At Loulan the surface is level and relatively smooth with evidence of only a few drainage channels (Fig. 2d). The value of $\bar{\theta}$ in this region is the smallest amongst the three land surfaces. As shown in Fig. 2 at the macroscale, point E is flatter than the sand dune areas (points B and A) but it is difficult to separate it from point C because both sites are relatively smooth. However, at the microscale (cm), point E is rougher than the Loulan surface because the particle size of point E is much larger than point C. This is consistent with the moderate magnitude of $\bar{\theta}$ values for point E (larger than point C but smaller than points A and B). In contrast, we would expect to find the largest average slope angle for the Taklimakan and Kumtag Desert locations because there are undulating sand dunes within the pixel. However, the sand dunes are different from each other (points A and B). Observations from the CBERS image (Fig. 2a) show that sand dunes of point A are approximately 200–600 m wide and the interdune distances are 300–1200 m wide. The sand dunes of point B are higher and the interdunes are narrower than those of the Taklimakan Desert. This indicates that $\bar{\theta}$ can differentiate the flat surface (Loulan) from the undulating topography of the dunes but it appears unable to discriminate the differences in dune characteristics such as dune height, width, slope, spacing, and orientation. It may be that multiple azimuth view and illumination angles are required to maximize the information content of the retrieved characteristics (Chappell et al., in press). This could only be obtained from multiple satellites because MISR flies in a sun-synchronous descending polar orbit and hence it crosses the equator always at 10:30 am local time. Our analyses incorporated only one azimuth illumination and azimuth viewing angle and further investigations are beyond the scope of this study. Nevertheless, $\bar{\theta}$ revealed the integral roughness of desert areas at sensor sub-pixel scales, at least in a relative sense.

The particle size of soils and deserts for the research area is much larger than the wavelengths of solar radiation. According to the scattering theory, the phase functions should be strongly forward scattered. Surprisingly, point C exhibits backward scattering. Mishchenko (1994) commented that the apparent backscattering in Hapke's model is an artifact of the numerical solutions of the radiative transfer equation for independently scattering particles. Despite this the backward-facing camera of point C does exhibit larger reflectance than the forward-facing camera (Fig. 5c). Unlike point B, point C is relatively flat without big dunes. Close packing of particles modifies the scattering by single particles. This backscattering appears to be due to shadow hiding caused by microscale surface roughness, which has been explained by numerous laboratory investigations (Hapke, 1993; Kamei & Nakamura, 2002; Shepard & Helfenstein, 2007). Its cause by coherent backscattering is usually limited to phase angles less than 2° (e.g., Hapke, 2002; Shepard & Helfenstein, 2007). This factor is unlikely to influence the opposition effect in our case because the smallest phase angle provided by MISR in this study was 30°.

Rough surfaces are usually believed to be more backward scattering (towards the illumination source) than smooth surfaces. Based on this evidence, empirical methods using the normalized index of backward-scattered radiance minus forward-scattered radiance have been used as an indicator of surface roughness (e.g., Chen et al., 2003, 2005; Nolin & Payne, 2007). In this study, the asymmetry factor had the largest negative values at Loulan which indicated the strongest backward scattering of light despite this location having the smoothest surface (smallest $\bar{\theta}$). The asymmetry factor values at the desert locations were also somewhat unexpected. In the Kumtag Desert, except point E, the scattering was largely mixed (neither predominantly backward nor forward scattering) despite the poorly compacted surface and large dunes. In the Taklimakan Desert scattering of light was predominantly backward despite the surface having a mixture of small dunes and large amounts of smooth interdune areas (Fig. 5a). The apparently contradictory asymmetry values for the three land surfaces may be due to the mixtures within the pixel of rising and falling sand ripples and oriented facets of sand dunes that modify the angular pattern of reflected radiation. This factor is different from the microscale roughness causing shadow hiding mentioned in the last paragraph. The roughness scale of dunes can be attributed to macroscale roughness and modifies the BRF of the desert surface. A similar phenomenon was observed by Warren and Brandt (1998) who documented the effects of sastrugi on reflectance anisotropy for the Antarctic ice sheet.

On the whole, particles with large values of single scattering albedo tend to be more transparent than those with small albedo and consequently we might expect them to be more forward scattering. However, at Loulan the single scattering albedo of the surface is the largest and has the strongest backward scattering. Point E, which has the smallest single scattering albedo among the four points, exhibits moderate backward scattering. This further suggests the effect of macroscale surface roughness. Although point E is smooth relative to points A and B, it still contains large-scale undulation compared to Loulan (Fig. 2c). Our results indicate that the isotropic Hapke model tends to smooth out anisotropic light scattering from the desert surfaces to the extent that it may even reduce the microscale effect. To resolve this problem, more work is required to understand the spatial scale at which roughness is detected by angular sensors and how solar illumination and feature orientation are important. In any case, our results demonstrate that at the sensor scale, a rough surface does not necessarily produce more backward scattering than a smooth surface, and vice versa. This finding has significant implications for empirical methods which should be used carefully for analyzing surface roughness from the remote sensing data, at least in arid areas.

5. Conclusions

We investigated the potential of multi-angle remotely sensed data to retrieve photometric properties of desert areas. We verified that physically interpretable properties can be derived from MISR data using the most recent Hapke macroscopic model. The retrieved results were largely affected by the initial value. To combat this problem we used a Monte Carlo method with physical constraints and a conformity indicator to ensure physically meaningful inversion. Two inversion experiments with both the full parameter set and the reduced parameter set (ω, b, c, and $\bar{\theta}$) neglecting opposition surge were conducted to help validate the correctness of the retrieved values. The results showed that the angular domain of the MISR sensor is sufficiently large to confidently determine the optimal values of Hapke's photometric parameters with the exception of the h parameter.

Retrieved values for the single scattering albedo ω were largest at Loulan, moderate in the Taklimakan Desert and smallest in the Kumtag Desert. These findings are consistent with observations that Loulan comprises aeolian sandy soils, the Taklimakan contains aeolian sandy soils and small sand dunes, and the Kumtag Desert is dominated by sand dunes with coarse grain size. Retrieved values for the macroscopic roughness parameter $\bar{\theta}$ in the two deserts are much larger than those at Loulan which suggests that $\bar{\theta}$ reveals the integral roughness of desert areas at sensor sub-pixel scales. Loulan had the largest retrieved values of the negative asymmetry factor but the

smallest roughness of all sites. The Taklimakan Desert and the relatively smooth areas of the Kumtag Desert exhibited moderately negative asymmetry factor values. In contrast, the sand dune area of the Kumtag Desert, which has the greatest roughness among the four points, had only slightly negative asymmetry factor values. These findings indicated that the Loulan soil surface was smoother than the desert sites at the macroscopic scales, and at the sensor scale, a rough surface (e.g., dunes) does not necessarily mean more backward scattering than a smooth surface. This finding has significant implications for empirical methods (e.g., using the normalized index of backward-scattered radiance minus forward-scattered radiance as an indicator to indicate surface roughness) which should be used carefully for analyzing surface roughness from the remote sensing data. Future research is needed to 1) understand how surface roughness at the sub-pixel scale modifies the angular characteristics of reflectance and to 2) find practical methods for rapid whole image processing for mapping the photometric parameters.

Acknowledgements

The authors are grateful for the MISR data provided by the NASA Langley Research Center Atmospheric Science Data Center and to Prof. Paul Helfenstein for providing his computer code which we subsequently modified. We would also like to thank Prof. Bruce Hapke for helpful suggestions on the manuscript and Prof. Xunming Wang (Cold and Arid Regions Environmental and Engineering Research Institute, Chinese Academy of Science), Prof. Huaidong Wei (Gansu Desert Control Research Institute), and Prof. Hujun Liu (Gansu Desert Control Research Institute) for providing much valuable information on the research area. We are also grateful for the comments of the anonymous reviewers. Any omissions or inaccuracies that remain in the paper are the sole responsibility of the authors. This study was financially supported by the National Natural Science Foundation of China (Grants 40701125), Hundred Talent Project of the Chinese Academy of Sciences, Chinese Post-doctoral Foundation (Grants 20060390537) and the Chinese Academy of Sciences K.C. Wong Post-doctoral Fellowships.

References

Bothwell, G. W., Hansen, E. G., Vargo, R. E., & Miller, K. C. (2002). The Multiangle Imaging SpectroRadiometer science data system, its products, tools and performance. *IEEE Transactions on Geoscience and Remote Sensing*, *40*, 1467–1476.

Chappell, A., Zobeck, T., & Brunner, G. (2006). Using bi-directional soil spectral reflectance to model soil surface changes induced by rainfall and wind-tunnel abrasion. *Remote Sensing of Environment*, *102*, 328–343.

Chappell, A., Strong, C., McTainsh, G., & Leys, J. (2007). Detecting induced in situ erodibility of a dust-producing playa in Australia using a bi-directional soil spectral reflectance model. *Remote Sensing of Environment*, *106*, 508–524.

Chappell, A., Leys, J., McTainsh, G., Strong, C. & Zobeck, T. (in press). Simulating Multi-angle Imaging Spectro-Radiometer (MISR) sampling and retrieval of soil surface roughness and composition changes using a bi-directional soil spectral reflectance model. J. Hill and A. Röder (Ed.) Advances in Remote Sensing and Geoinformation Processing for Land Degradation Assessment. Taylor and Francis, The Netherlands.

Chen, J. M., Liu, J., Leblanc, S. G., Lacaze, R., & Roujean, J. L. (2003). Multi-angular optical remote sensing for assessing vegetation structure and carbon absorption. *Remote Sensing of Environment*, *84*, 516–525.

Chen, J. M., Menges, C. H., & Leblanc, S. G. (2005). Global mapping of foliage clumping index using multi-angular satellite data. *Remote Sensing of Environment*, *97*, 447–457.

Chopping, M. J., Su, L., Rango, A., Martonchik, J. V., Peters, D. P. C., & Laliberte, A. (2007). Remote sensing of woody shrub cover in desert grasslands using MISR with a geometric-optical canopy reflectance model. *Remote Sensing of Environment*, *112*, 19–34.

Clark, B. E., Helfenstein, P., Bell, J. F., III, Veverka, J., Izenberg, N. I., Domingue, D., Wellnitz, D., & McFadden, L. A. (2002). NEAR infrared spectrometer photometry of Asteroid 433 Eros. *Icarus*, *155*, 189–204.

Cord, A. M., Pinet, P. C., Daydou, Y., & Chevrel, S. D. (2003). Planetary regolith surface analogs: optimized determination of Hapke parameters using multi-angular spectro-imaging laboratory data. *Icarus*, *165*, 414–427.

Cooper, K. D., & Smith, J. A. (1985). A Monte Carlo reflectance model for soil surfaces with three-dimensional structure. *IEEE Transactions on Geoscience and Remote Sensing*, *23*, 668–673.

Deering, D. W., Eck, T. F., & Otterman, J. (1990). Bidirectional reflectances of selected desert surfaces and their three-parameter soil characterization. *Agricultural and Forest Meteorology*, *52*, 71–93.

Diner, D. J., Beckert, J. C., Reilly, T. H., Bruegge, C. J., Conel, J. E., Kahn, R. A., et al. (1998). Multi-angle Imaging SpectroRadiometer (MISR) instrument description and experiment overview. *IEEE Transactions on Geoscience and Remote Sensing*, *36*, 1072–1087.

Ding, Z. L., Derbyshire, E., Yang, S. L., Sun, J. M., & Liu, T. S. (2005). Stepwise expansion of desert environment across northern China in the past 3.5 Ma and implications for monsoon evolution. *Earth and Planetary Science Letters*, *237*, 45–55.

Escadafal, R. (1989). Caracterisation de la surface des sols arides par observations deterrain et teledetection. These de Doctorat es Sciences, Universite Paris VI, publiee par Collection Etudes et Theses, Editions de l'ORSTOM, Bondy, France, 317 pp.

Grubbs, F. (1969). Procedures for detecting outlying observations in samples. *Technometrics*, *11*(1), 1–21.

Hapke, B. (1981). Bidirectional reflectance spectroscopy. 1. Theory. *Journal of Geophysical Research*, *86*, 3039–3054.

Hapke, B. (1984). Bidirectional reflectance spectroscopy. 3. Correction for macroscopic roughness. *Icarus*, *59*, 41–59.

Hapke, B. (1993). *Theory of reflectance and emittance spectroscopy*. Cambridge, UK: Cambridge Univ. Press.

Hapke, B. (2002). Bidirectional reflectance spectroscopy 5. The coherent backscatter opposition effect and anisotropic scattering. *Icarus*, *157*, 523–534.

Helfenstein, P., & Veverka, J. (1987). Photometric properties of lunar terrains derived from Hapke's equation. *Icarus*, *72*, 342–357.

Jacquemoud, S., Bater, F., & Hanocq, J. F. (1992). Modeling spectral and bidirectional soil reflectance. *Remote Sensing of Environment*, *41*, 123–132.

Kamei, A., & Nakamura, A. M. (2002). Laboratory study of the bidirectional reflectance of powdered surfaces: on the asymmetry parameter of asteroid photometric data. *Icarus*, *156*, 551–561.

Karnieli, A., & Cierniewski, J. (2001). Inferring the roughness of desert rocky surfaces from their bidirectional reflectance data. *Advances in Space Research*, *28*, 171–176.

Laurent, B., Marticorena, B., Bergametti, G., Chazette, P., Maignan, F., & Schmechtig, C. (2005). Simulation of the mineral dust emission frequencies from desert areas of China and Mongolia using an aerodynamic roughness length map derived from the POLDER/ADEOS 1 surface products. *Journal of Geographical Research*, *110*, D18S04. doi:10.1029/2004JD005013

Li, X., Maring, H., Savole, D., Voss, K., & Prospero, J. M. (1996). Dominance of mineral dust in aerosol light-scattering in the North Atlantic trade winds. *Nature*, *380*, 416–419.

Li, Z., Barker, H., & Moreau, L. (1995). The variable effect of clouds on atmospheric absorption of solar radiation. *Nature (article)*, *376*, 486–490.

Liu, H., Wang, J., Liao, K., & Zheng, Q. (2006). Morphologic parameters of featherlike longitudinal ridge of Kumtag Desert.*Arid Land Geography*, *29*, 314–320 (in Chinese).

Marticorena, B., Chazette, P., Bergametti, G., Dulac, F., & Legrand, M. (2004). Mapping the aerodynamic roughness length of desert surfaces from the POLDER/ADEOS bi-directional reflectance product. *International Journal of. Remote Sensing*, *25*, 603–626.

McGuire, A. F., & Hapke, B. W. (1995). An experimental study of light scattering by large, irregular particles. *Icarus*, *113*, 134–155.

Mishchenko, M. I. (1994). Asymmetry parameters of the phase function for densely packed scattering grains. *Journal of Quantitative Spectroscopy & Radiative Transfer*, *52*, 95–110.

Mustard, J. F., & Pieters, C. M. (1989). Photometric phase functions of common geologic minerals and applications to quantitative analysis of mineral mixture reflectance spectra. *Journal of Geographical Research*, *94*(B10), 13619–13634.

Nolin, A. W., & Payne, M. C. (2007). Classification of glacier zones in western Greenland using albedo and surface roughness from the Multi-angle Imaging SpectroRadiometer (MISR). *Remote Sensing of Environment*, *104*, 264–275.

Piatek, J. L., Hapke, B. W., Nelson, R. M., Smythe, W. D., & Hale, A. S. (2004). Scattering properties of planetary regolith analogs. *Icarus*, *171*, 531–545.

Pinty, B., Verstraete, M. M., & Dickinson, R. E. (1989). A physical model for predicting bidirectional reflectances over bare soil. *Remote Sensing of Environment*, *27*, 273–288.

Pinty, B., Widlowski, J. L., Gobron, N., Verstraete, M. M., & Diner, D. J. (2002). Uniqueness of multiangular measurements — Part I: An indicator of subpixel surface heterogeneity from MISR. *IEEE Transactions on Geoscience and Remote Sensing*, *40*(7), 1560–1573.

Privette, J. L., Myneni, R. B., Emery, W. J., & Pinty, B. (1995). Inversion of a soil bidirectional reflectance model for use with vegetation reflectance models. *Journal of Geophysical Research*, *100*(D12), 25497–25508.

Shepard, M. K., & Helfenstein, P. (2007). A test of the Hapke photometric model. *Journal of Geophysical Research*, *112*, E03001. doi:10.1029/2005JE002625

Shoshany, M. (1993). Roughness–reflectance relationships of bare desert terrain: An empirical study. *Remote Sensing of Environment*, *45*, 15–27.

Stefansky, W. (1972). Rejecting outliers in factorial designs. *Technometrics*, *14*, 469–479.

Wang, X. M., Dong, Z., Zhang, J., & Chen, G. (2002). Geomorphology of sand dunes in the Northeast Taklimakan Desert. *Geomorphology*, *42*, 183–195.

Warren, S. G., & Brandt, R. E. (1998). Effect of surface roughness on bidirectional reflectance of Antarctic snow. *Journal of Geophysical Research*, 25789–25807.

Wei, H., Wang, J., Xu, X., & Ding, F. (2007). Analysis of grain size of different sand dunes types in Kumtag Desert.*Journal of Soil and Water Conservation*, *21*(3), 6–9 (in Chinese).